

Sparse synthetic aperture with Fresnel elements (S-SAFE) using digital incoherent holograms

Yuval Kashter,^{1,*} Yair Rivenson,² Adrian Stern,³ and Joseph Rosen¹

¹Department of Electrical and Computer Engineering, Ben-Gurion University of the Negev, P.O. Box 653, Beer-Sheva 8410501, Israel

²Faculty of Engineering, Bar-Ilan University, 5290002, Ramat-Gan, Israel

³Department of Electro-Optics Engineering, Ben-Gurion University of the Negev, P.O. Box 653, Beer-Sheva 8410501, Israel

*kashter@ee.bgu.ac.il

Abstract: Creating a large-scale synthetic aperture makes it possible to break the resolution boundaries dictated by the wave nature of light of common optical systems. However, their implementation is challenging, since the generation of a large size continuous mosaic synthetic aperture composed of many patterns is complicated in terms of both phase matching and time-multiplexing duration. In this study we present an advanced configuration for an incoherent holographic imaging system with super resolution qualities that creates a partial synthetic aperture. The new system, termed sparse synthetic aperture with Fresnel elements (S-SAFE), enables significantly decreasing the number of the recorded elements, and it is free from positional constraints on their location. Additionally, in order to obtain the best image quality we propose an optimal mosaicking structure derived on the basis of physical and numerical considerations, and introduce three reconstruction approaches which are compared and discussed. The super-resolution capabilities of the proposed scheme and its limitations are analyzed, numerically simulated and experimentally demonstrated.

©2015 Optical Society of America

OCIS codes: (070.0070) Fourier optics and signal processing; (090.0090) Holography; (090.1995) Digital holography; (280.6730) Synthetic aperture radar; (050.1965) Diffractive lenses; (050.5080) Phase shift; (090.2890) Holographic optical elements; (110.3175) Interferometric imaging; (100.3190) Inverse problems; (110.1758) Computational imaging.

References and links

1. E. Abbe, "Beiträge zur theorie des mikroskops und der mikroskopischen wahrnehmung," *Archiv. Mikroskopische Anat.* **9**(1), 413–418 (1873).
2. A. A. Michelson, "On the application of interference methods to astronomical measurements," *Astrophys. J.* **51**, 257–262 (1920).
3. P. R. Lawson, *Selected Paper on Long Baseline Stellar Interferometry* (SPIE Press Book, 1997).
4. S. M. Beck, J. R. Buck, W. F. Buell, R. P. Dickinson, D. A. Kozłowski, N. J. Marechal, and T. J. Wright, "Synthetic-aperture imaging laser radar: laboratory demonstration and signal processing," *Appl. Opt.* **44**(35), 7621–7629 (2005).
5. V. Micó, Z. Zalevsky, P. García-Martínez, and J. García, "Synthetic aperture superresolution with multiple off-axis holograms," *J. Opt. Soc. Am. A* **23**(12), 3162–3170 (2006).
6. G. Indebetouw, Y. Tada, J. Rosen, and G. Brooker, "Scanning holographic microscopy with resolution exceeding the Rayleigh limit of the objective by superposition of off-axis holograms," *Appl. Opt.* **46**(6), 993–1000 (2007).
7. L. Martínez-León and B. Javidi, "Synthetic aperture single-exposure on-axis digital holography," *Opt. Express* **16**(1), 161–169 (2008).
8. L. Granero, V. Micó, Z. Zalevsky, and J. García, "Synthetic aperture superresolved microscopy in digital lensless Fourier holography by time and angular multiplexing of the object information," *Appl. Opt.* **49**(5), 845–857 (2010).
9. K. Ji, P. Gao, J. Min, R. Guo, and N. Menke, "A synthetic aperture telescope based on a pair of gratings," *J. Mod. Opt.* **60**(15), 1229–1233 (2013).
10. B. Katz and J. Rosen, "Super-resolution in incoherent optical imaging using synthetic aperture with Fresnel elements," *Opt. Express* **18**(2), 962–972 (2010).
11. J. Rosen and G. Brooker, "Digital spatially incoherent Fresnel holography," *Opt. Lett.* **32**(8), 912–914 (2007).

12. J. Rosen and G. Brooker, "Non-scanning motionless fluorescence three-dimensional holographic microscopy," *Nat. Photonics* **2**(3), 190–195 (2008).
13. B. Katz and J. Rosen, "Could SAFE concept be applied for designing a new synthetic aperture telescope?" *Opt. Express* **19**(6), 4924–4936 (2011).
14. Y. Kashter and J. Rosen, "Enhanced-resolution using modified configuration of Fresnel incoherent holographic recorder with synthetic aperture," *Opt. Express* **22**(17), 20551–20565 (2014).
15. J. Rosen, N. Siegel, and G. Brooker, "Theoretical and experimental demonstration of resolution beyond the Rayleigh limit by FINCH fluorescence microscopic imaging," *Opt. Express* **19**(27), 26249–26268 (2011).
16. B. Katz, J. Rosen, R. Kelner, and G. Brooker, "Enhanced resolution and throughput of Fresnel incoherent correlation holography (FINCH) using dual diffractive lenses on a spatial light modulator (SLM)," *Opt. Express* **20**(8), 9109–9121 (2012).
17. A. E. Tippie, A. Kumar, and J. R. Fienup, "High-resolution synthetic-aperture digital holography with digital phase and pupil correction," *Opt. Express* **19**(13), 12027–12038 (2011).
18. N. J. Miller, M. P. Dierking and B. D. Duncan, "Optical sparse aperture imaging," *Appl. Opt.* **46**(23), 0003–6935(2007).
19. Y. Rivenson, A. Stern, and B. Javidi, "Compressive Fresnel holography," *J. Disp. Technol.* **6**(10), 506–509 (2010).
20. E. Candès and J. Romberg, "Sparsity and incoherence in compressive sampling," *Inverse Probl.* **23**(3), 969–985 (2007).
21. E. Candès and M. Wakin, "An introduction to compressive sampling," *IEEE Signal Process. Mag.* **25**(2), 21–30 (2008).
22. G. Brooker, N. Siegel, V. Wang, and J. Rosen, "Optimal resolution in Fresnel incoherent correlation holographic fluorescence microscopy," *Opt. Express* **19**(6), 5047–5062 (2011).
23. J. W. Goodman, *Introduction to Fourier optics, 3rd Ed.* (Roberts and Company Publishers, 2005).
24. Y. Rivenson, A. Stern, and B. Javidi, "Overview of compressive sensing techniques applied in holography [Invited]," *Appl. Opt.* **52**(1), A423–A432 (2013).
25. J. M. Bioucas-Dias and M. A. T. Figueiredo, "A new TwIST: two-step iterative shrinkage/thresholding algorithms for image restoration," *IEEE Trans. Image Process.* **16**(12), 2992–3004 (2007).
26. P. Chatterjee, S. Mukherjee, S. Chaudhuri, and G. Seetharaman, "Application of Papoulis-Gerchberg method in image super-resolution and inpainting," *Comput. J.* **52**(1), 80–89 (2009).
27. Y. Rivenson, A. Rot, S. Balber, A. Stern, and J. Rosen, "Recovery of partially occluded objects by applying compressive Fresnel holography," *Opt. Lett.* **37**(10), 1757–1759 (2012).
28. B. K. Jennison, J. P. Allebach, and D. W. Sweeney, "Iterative approaches to computer-generated holography," *Opt. Eng.* **28**(6), 286629 (1989).

1. Introduction

The ultimate goal of many optical imaging technologies is to produce images of very distant or very small objects. Since the resolving power of a conventional diffraction-limited optical imaging system is determined by its aperture size [1], high resolution must be sacrificed to achieve a compact sized system or vice versa. Therefore, the desire to achieve ultra-fine angular resolution in conventional imaging systems demands a relatively large aperture size, which might become challenging in terms of weight, structure stability and cost.

The optical synthetic aperture (SA) concept is the basis of a well-known technique that provides the ability to magnify the resolving power beyond the diffraction limit [2–9]. In this technique, several interference patterns (interferograms) are captured by an aperture-limited system from various viewpoints. These interferograms, referred to as sub-holograms, are tiled into a new larger pattern, which can be considered to have been formed by a virtual equivalent imaging system with a much wider aperture [5–9]. This approach enlarges the effective aperture of the system, which is now equivalent to an imaging system with a higher numerical aperture (NA) value.

Holographic imaging methods are frequently utilized in order to realize the SA principle, since they enable implementing the above-mentioned tiling of interference patterns [5–9]. However, these methods are usually restricted to cases where coherent illumination is used. For example, the proposal by Granero et al. [8] uses a digital Fourier holographic architecture, implemented with tilted laser beam illumination and interferometric recording to achieve super-resolution in microscopy. However, the use of lasers introduces challenges in terms of power requirements and may be restricted by practical limitations in the sense that not all the observed objects can be illuminated by a laser, especially in the case of telescopic

applications. Hence, an SA based on incoherent light illumination could be more effective for many applications.

Recently, a new type of imaging system with super-resolution capabilities has been proposed by Katz and Rosen, dubbed synthetic aperture with Fresnel elements (SAFE) [10]. This method is based on the recently developed non-scanning, incoherent holographic system, called Fresnel incoherent correlation holography (FINCH) [11,12]. SAFE creates an SA by combining several Fresnel sub-holograms captured from various viewpoints by FINCH with a limited physical aperture. Later on, another scheme of SAFE was proposed, dubbed Telescopic SAFE (T-SAFE) [13]. In T-SAFE, due to modifications of the original SAFE setup, the resolution has been improved by the ratio between the synthetic and the physical aperture sizes. In a recent study regarding SA techniques, Kashter and Rosen proposed and demonstrated a modified SAFE configuration, dubbed dual lens SAFE [14], which enables reconstructing images with higher resolution from the SA holograms. In this method, the stitches between the sub-holograms never pass through the center of the mosaic hologram in order to reduce distortions in the reconstructed images. The implementation of this principle is carried out in two different configurations, one for the central holographic Fresnel element and the other for the additional peripheral sub-elements. The configuration of the central element in the dual lens SAFE scheme is actually a dual lens FINCH scheme [15,16], whereas the configuration of the additional sub-elements consists of two optical channels, each of which is equipped with diffractive, or refractive, elements. In all the experiments performed with SAFE so far [10,13,14], the various diffractive elements have been implemented using phase-only spatial light modulators (SLMs). In dual lens SAFE, for every object point the interference occurs between two closely spaced spherical waves with different curve radii, rather than between spherical and plane waves, as was done in Refs [10–13]. In addition, a new simple technique to tile the sub-holograms into a large synthetic hologram, called the true position calibration technique (TPCT), has been presented and demonstrated in [14]. The ability of dual lens SAFE to reconstruct an image with super-resolution capabilities was experimentally demonstrated, where an object illuminated by an incoherent light source was imaged. The results indicate that it is possible to perceive additional fine details in the reconstructed image, which otherwise can be revealed only by the use of an aperture of larger size than the physical aperture of each element in the dual lens SAFE setup. In addition, the artifacts occurring due to the stitches between the holographic elements are minimized relative to previous versions of SAFE [10,13].

In principle, it is possible to create a large scale effective aperture consisting of many sub-holograms with relatively small sized apertures. However, in practice, the task becomes extremely complicated due to the requirement of tiling a large number of sub holograms into a complete continuous mosaic hologram. Moreover, in order to enable the continuity of the large scale mosaic hologram, without opaque areas and without any overlapping between different sub holograms, one needs to position the couples of SLMs with very high accuracy. As the number of the interferograms increases, the system's tolerance (regarding the aperture positions) becomes tighter, especially when illumination with relatively short optical wavelengths (e.g. the visible spectrum) is used [17]. Consequently, a large SA demands many measurements with severe mechanical constrains, which makes the method extremely challenging and sometimes even impossible. Recently, Tippie et al. [17] have shown that the residual wave-front errors that occur due to geometry mismatches can be overcome using phase correction algorithms, and demonstrated this capability with their 218 mega-pixel SA.

Alternatively, a FINCH based sparse SA configuration, meaning a partial mosaic hologram with interferograms that are not constrained to any particular positions, enables using a practical large SA under incoherent light illumination in a simple way and without phase correction algorithms. An example of enhanced resolution by sparse aperture incoherent imaging is given in [18], where a sparse aperture array provides better resolution

compared with a monolithic aperture with equal total area. However, this method is limited by the need to maintain accurate phase relationships between the separated sub-apertures.

A recent study introduced compressive Fresnel holography (CFH) [19] and presented the ability to reconstruct an object from its subsampled Fresnel hologram, using the compressive sensing (CS) approach [20,21]. In CFH, when a Fresnel hologram is sampled randomly, but with a sample density decreasing from the center towards the perimeter, the recorded object can be properly reconstructed using the CS algorithm. On the other hand, with the same algorithms, a random pattern with a uniform sampling density provides inferior performance in terms of reconstruction quality for typical objects.

In this study, inspired by CFH and based on the modified SAFE concept, we present and demonstrate a new method of sparse SA that provides relatively high image resolution for the observed objects. We call the proposed method sparse synthetic aperture with Fresnel elements (S-SAFE). In the next sections the S-SAFE system and its properties are analyzed and demonstrated as follows. In section 2.1, the main methodology of S-SAFE, based on the principle of the modified SAFE scheme, is presented briefly. A detailed mathematical analysis of S-SAFE is provided in the Appendix. In section 2.2, the algorithms of numerical Fresnel back propagation (FBP), CS and Papoulis-Gerchberg (PG) are presented as three reconstruction approaches, where CS and PG enable overcoming the sparsity effect caused by the missing aperture parts. In section 2.3, two considerations regarding the mosaicking structure are presented and explained. In section 3.1, the ability to reconstruct a partial mosaic hologram is examined with numerical simulations using the three above mentioned techniques. In section 3.2, the number of the samples required to reconstruct a sparse SA is empirically investigated. In section 3.3, the main experimental procedure is conducted, where a real partial mosaic hologram is acquired and reconstructed by the three above mentioned approaches. This procedure demonstrates the ability to implement the S-SAFE principle in practice.

2. Methods and analysis

2.1 The concept of S-SAFE

In this section we describe the S-SAFE system and analyze its performance. Following [14], it is assumed that the observed scene contains spatially bounded objects, the center of mass of the observed scene is close to the optical axis and most of the object energy is concentrated in a relatively small area near the optical axis. Under these assumptions, the importance of creating a continuous central holographic region is emphasized in [14]. Explicitly, a major amount of the intensity emitted from the natural objects propagates towards the optical system within a relatively small angular aperture around the optical axis, and thus any discontinuity through the central sub-hologram leads to highly distorting effects in the reconstructed image. Furthermore, the central, continuous region of interest is determined to be the area in which most of the energy at the hologram plane is confined. The higher spatial frequencies of the object are mostly recorded in the marginal sub holographic elements around the central element and are used to improve the imaging resolution. In the present study, similarly to [14], the central sub-hologram is recorded by an ordinary FINCH [22] system in order to generate a continuous central element [see Fig. 1 (a)].

In the early version of FINCH [11,12], each object point is split into a plane wave and a spherical wave before interfering on the camera plane. In the more advanced version, termed dual-lens FINCH, two closely spaced spherical waves with different curve radii are created from each object point and then interfered on the camera plane [16]. The dual-lens FINCH system can operate with wider bandwidth light sources than in the former system. However, for the sake of simplicity, here we analyze and demonstrate S-SAFE of the former type, in which every point source induces plane and spherical waves that interfere on the hologram plane. To keep the maximal optical path difference between the waves passing through the

system below the coherence length, a band pass filter (BPF) is positioned at the system input. Nevertheless, if the wide bandwidth light source cannot be filtered chromatically, decreasing the maximal path difference is possible by using an additional refractive lens, as was demonstrated by the dual lens SAFE in [14].

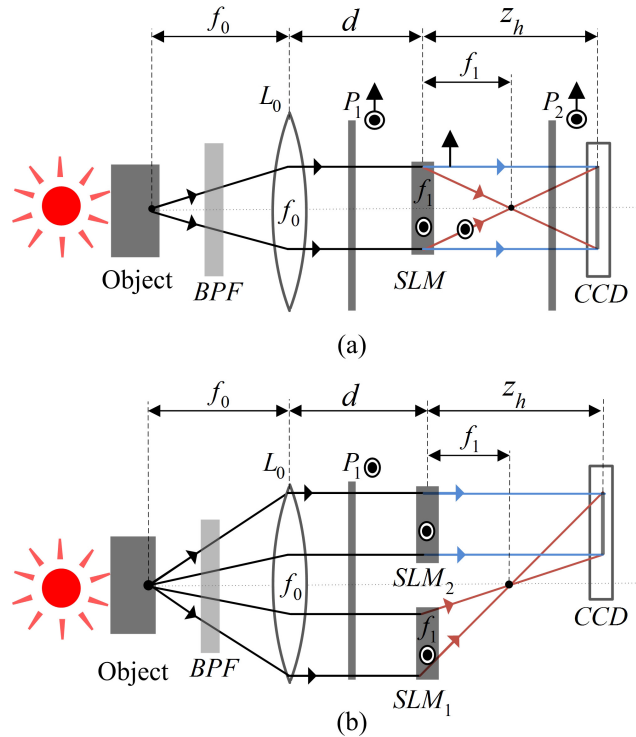


Fig. 1. Schematic configurations of S-SAFE system: L_0 collimation lens; P_1 and P_2 , polarizers; SLM, SLM_1 and SLM_2 , spatial light modulators; CCD, charged couple device; BPF, bandpass filter. These setups create (a) a continuous central holographic element by implementing the FINCH method, f_1 is the focal length of the diffractive lens displayed on the SLM (b) a marginal holographic element, where SLM_1 and SLM_2 are shifted in two symmetrical viewpoints in front of the collimation lens L_0 ; a diffractive lens with focal length f_1 is displayed on SLM_1 . The symbols \odot , \uparrow and \otimes represent polarization directions, perpendicular, parallel and 45° with respect to the plane of the page, respectively.

The central incoherent sub-hologram of an object point located on the front focal plane of a collimating lens L_0 , with the transverse position $\vec{r}_s = (x_s, y_s)$, is created in a single-channel system by the interference of a spherical wave and a plane wave; the first converges to a point positioned at a distance of f_1 from the SLM, and the second propagates through the SLM [See Fig. 1(a)]. It should be emphasized that the collimation lens L_0 converts the spherical wave emitted from the object point into a plane wave at the entrance of the system. Thus, the lens L_0 and the point source are employed here to simulate objects located at infinity and, therefore, assuming the SA is designed for objects at infinity, L_0 is not considered to be part of the holographic SA system. Following Ref [22], for maximum visibility of the interference between the two waves, two polarizers P_1 and P_2 , oriented at 45° with respect to the SLM active axis, should be positioned before and after the SLM. Based on the FINCH theory [15], to achieve optimal resolution, the two interfering beams should overlap on the camera plane. To fulfill this requirement, the distance between the SLM and the camera plane z_h should be twice the focal length f_1 of the diffractive lens displayed on the SLM, i.e. $z_h = 2f_1$. Following the first step of recording the central sub-hologram and, similarly, adhering to the previously defined SAFE procedures [10,13,14], the two SLMs, denoted SLM_1 and SLM_2 , are

symmetrically shifted in opposite directions away from the center. The two peripheral parts of the spherical wave emitted from the object point are directed by the two SLMs to interfere on the camera plane, enabling an additional sub-hologram to be recorded [Fig. 1(b)]. Contrary to the previous configurations, in S-SAFE only some of the peripheral sub-holograms are captured and the distance of the active SLMs from the optical axis (X_n, Y_n) is a random number [Fig. 2(b)]. Recording the non-central sub-holograms is carried out through two different optical channels and thus the polarization method of multiplexing interfering waves in a single channel is no longer needed. Therefore, in order to achieve maximal power efficiency in the peripheral sub-holograms, the exit polarizer P_2 is removed, whereas the entrance polarizer P_1 is adjusted to the same orientation as the active axis of the SLMs. This configuration creates interference between spherical and plane waves, propagating in two different channels, while the distance z_h is kept identical and is twice the focal length f_1 .

An analysis of the proposed system, based on the Fresnel propagation formula in the paraxial approximation [23], is provided in the appendix. Figure 2, illustrates the diffractive elements of the SLM and the acquisition principles used to acquire the central element [Fig. 2(a)], and the marginal elements [Fig. 2(b)] of S-SAFE, where $A_x \times A_y$ and $\tilde{A}_x \times \tilde{A}_y$ are the sizes of the central and marginal SLM apertures, respectively, and X_n and Y_n are random values representing the locations of conjugated SLM₁ and SLM₂ along the x and y axes. An example of the sample formation of an S-SAFE mosaic hologram is depicted in Fig. 2(c), where the white regions represent the active apertures on the measured hologram, and the diameter D_H represents the external boundary of the sparse mosaic hologram.

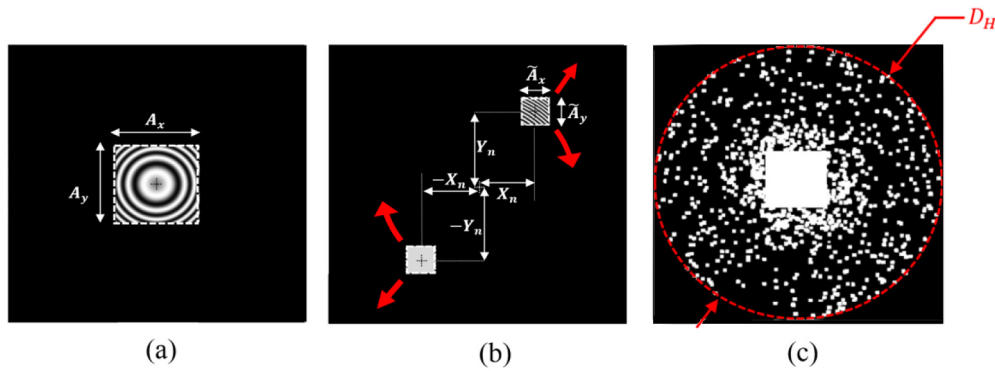


Fig. 2. (a) For the index $n = 0$, the central mask ($A_x \times A_y$ in size) consists of a diffractive lens with a focal length of f_1 . (b) For $n > 0$, two masks ($\tilde{A}_x \times \tilde{A}_y$ in size) are displayed on SLM₁ and SLM₂; one is a diffractive lens with a focal length of f_1 and the other has a constant phase. SLM₁ and SLM₂ are located at (X_n, Y_n) and $(-X_n, -Y_n)$, respectively. (c) An example for a sparse aperture of the recorded hologram. The diameter D_H represents the aperture of the total digital hologram. The red arrows in (b) represent radial and angular symmetrical movements of SLM₁ and SLM₂. In this example $A_{x,y} = 250$, $\tilde{A}_{x,y} = 17$, $D_H = 1024$ pixels.

The PSF $I(\vec{r}_0; \vec{r}_s; \theta_j)$ of the system for recording a Fresnel hologram is explained in detail in the appendix [Eq. (12)]. The partial mosaic Fresnel hologram of a general object with an intensity distribution of $I_s(\vec{r}_s)$, illuminated by an incoherent and quasi-monochromatic light source, is a convolution of the system PSF, given by Eq. (12) in the Appendix, with the object intensity distribution, as follows:

$$H(\vec{r}_0; \theta_j) = I_s(\vec{r}_s) * I(\vec{r}_0; \vec{r}_s; \theta_j), \quad (1)$$

where the asterisk denotes a 2D convolution, $\theta_j = 0, 120^\circ, 240^\circ$ represent three angles used for the phase shifting procedure, enabling to eliminate the twin image and the bias terms from the hologram [10–16], and $\vec{r}_0 = (x_0, y_0)$, $\vec{r}_s = (x_s, y_s)$ are the location vectors of the CCD and the input planes, respectively.

As mentioned in the early FINCH studies [11], a final hologram is given by the superposition of three recorded holograms captured with the three above mentioned different θ_j angles as follows:

$$\begin{aligned} u_H(\vec{r}_0) = & H(\vec{r}_0; \theta_1) [\exp(-i\theta_3) - \exp(-i\theta_2)] \\ & + H(\vec{r}_0; \theta_2) [\exp(-i\theta_1) - \exp(-i\theta_3)] \\ & + H(\vec{r}_0; \theta_3) [\exp(-i\theta_2) - \exp(-i\theta_1)], \end{aligned} \quad (2)$$

where u_H represents the final computed hologram.

To tile the sub-holograms in their appropriate positions, the above mentioned TPCT [14] is implemented. Explicitly, the exact position of each sub-hologram is determined according to the rule that the final mosaic hologram of an object point should be reconstructed to the sharpest image point. Once the particular positions of the elements are determined, an appropriate $M_X \times M_Y$ binary mask, Λ , representing the sparse active areas of the aperture, is defined. Examples of such binary masks are shown in Figs. 2(c) and 3(b).

2.2 Reconstruction approaches

2.2.1 Fresnel back propagation (FBP)

FBP is the conventional method of reconstructing any digital Fresnel hologram by calculating the convolution of the hologram function with a quadratic phase function dependent on the reconstruction distance z_r , as follows [12,13,15,16]:

$$u_{REC} = u_H * Q \left[-\frac{1}{z_r} \right], \quad (3)$$

where u_{REC} represents the reconstructed image and Q designates the quadratic phase function of the form: $Q(b) = \exp[i\pi b \lambda^{-1}(x^2 + y^2)]$, where λ is the central wavelength of the light source. However, one can recognize that the effect of the hologram sparsity, and consequently the missing data, creates a distorted reconstructed image. Therefore, in the following we present two additional reconstruction approaches which are aimed at improving the image quality reconstructed from the sparse hologram.

2.2.2 Compressive sensing (CS)

CS [19–21] is a method, which provides mathematical guarantees for the reconstruction of what was classically considered an undersampled signal. Thus, it fits the present framework, in which high resolution objects should be reconstructed from a sparse array of apertures. The CS framework basically needs two ingredients. The first one is signal sparsity, either explicitly or implicitly, by using an arbitrary transform. The second one is the creation of an appropriate sensing mechanism; the object needs to be projected onto a signal space (e.g. Fourier space, random Gaussian projections, etc.) that holds low similarity, also known as incoherence, with the sparse basis of the input signal [19–21]. These two requirements are typically satisfied in holography [24]. Therefore, under these two assumptions, the sensing process can be formulated as a forward operator describing the sparse hologram of an input signal in terms of convolution and data discarding as follows:

$$u_H = \Lambda \cdot \left\{ f * Q \left[\frac{1}{z_r} \right] \right\}, \quad (4)$$

where Λ is the above mentioned $M_x \times M_y$ binary mask representing the active regions on the SA and f is the two dimensional object signal. In other words, Eq. (4) describes a Fresnel hologram, down-sampled by the binary random mask Λ . To meet the under-sampled sensing condition, the number of the active pixels of the binary matrix Λ should satisfy the condition $\sum_{q=1}^{M_x} \sum_{p=1}^{M_y} \Lambda(q, p) < M_x \cdot M_y$. Figure 3(a) shows a Fresnel hologram of an object point, whereas an example of the random binary mask Λ is illustrated in Fig. 3(b). From the corresponding sparse hologram of the object point [presented in Fig. 3(c)], one can realize that the PSF energy spreads across all the measurements (sub-apertures) in the hologram space. According to the CS theorem, the effects of the missing data can be minimized by solving a minimization problem formulated with respect to the total variation (TV) minimization, which is commonly used in classical CS problems [19–21], as follows:

$$\min_f TV(\hat{f}) \quad s.t. \quad \hat{f} = u_H * Q \left[-\frac{1}{z_r} \right], \quad (5)$$

where $TV(\hat{f}) = \sum_{i,j} \sqrt{(\hat{f}_{i+1,j} - \hat{f}_{i,j})^2 + (\hat{f}_{i,j+1} - \hat{f}_{i,j})^2}$ represents the total variation and \hat{f} represents the reconstructed image. For example, a sparse hologram (size of 1080×1080 pixels) of an object point [Fig. 3(c)] is reconstructed by FBP and CS techniques. In Fig. 3(d) the reconstruction obtained by FBP creates a noisy object point, whereas reconstruction through an iterative estimation creates a sharper point object, as shown in Fig. 3(e). The estimation is produced by employing an iterative solver, called the two step iterative shrinkage/thresholding (TwIST) algorithm [25], on the problem described by Eq. (5).

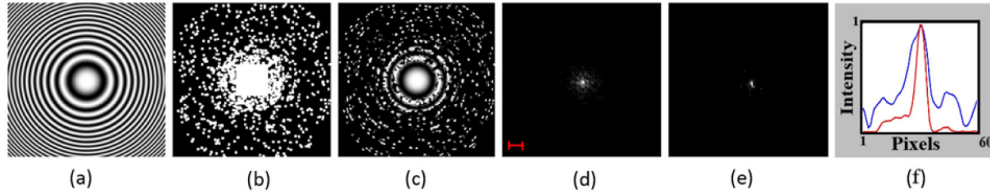


Fig. 3. Example of sparse holographic imaging of an object point: (a) a complete hologram of an object point; (b) an example of the mask Λ ; (c) a sparse hologram; (d) a reconstructed image using FBP; (e) a reconstructed image using the TwIST algorithm; (f) The horizontal cross-sections intensity of the images in (d) and (e). The blue and the red colors represent the FBP and CS reconstructions, respectively. The scale bar is 60 pixels.

2.2.3 Papoulis-Gerchberg (PG) extrapolation

The PG algorithm is another approach to reconstruct images from sparse holograms, where the algorithm herein is inspired by an iterative error energy reduction process used for super-resolution of images in general [26]. In order to satisfy the constrains of the algorithm, namely the measured sparse mosaic hologram u_H and its corresponding reconstructed image u_{REC} , the iterative PG algorithm consists of the following four steps (see Fig. 4):

- (i) Computing the Fresnel forward propagation (FFP) with respect to the distance z_r as follows:

$$u_{H_i} = u_{REC_i} * Q \left[\frac{1}{z_r} \right], \quad (6)$$

where u_{H_i} and u_{REC_i} represents a hologram and its corresponding reconstructed image, respectively, at the i_{th} iteration.

- (ii) Integrating the measured complex sparse hologram u_H with u_{H_i} . This step is done by two operations: first, u_{H_i} is multiplied by a complementary binary mask to Λ (see Fig. 4) and next the original complex sparse hologram u_H is added so:

$$\hat{u}_{H_i} = u_{H_i} \cdot (1 - \Lambda) + u_H. \quad (7)$$

- (iii) FBP according to Eq. (3).

- (iv) Multiplying the computed reconstructed image u_{REC_i} with a 2D rectangular window, S , defining the object spatial support.

The initial pattern $u_{initial}$ is an estimated reconstructed image obtained by performing FBP on the measured sparse SA with a random phase on its non-measured areas as follows:

$$u_{initial} = \left(\left\{ u_H + (1 - \Lambda) \cdot A e^{-i2\pi\varphi_{rand}} \right\} * \mathcal{Q} \left[-\frac{1}{z_r} \right] \right) \cdot S, \quad (8)$$

where A is a constant amplitude, and φ_{rand} is a random $M_x \times M_y$ matrix.

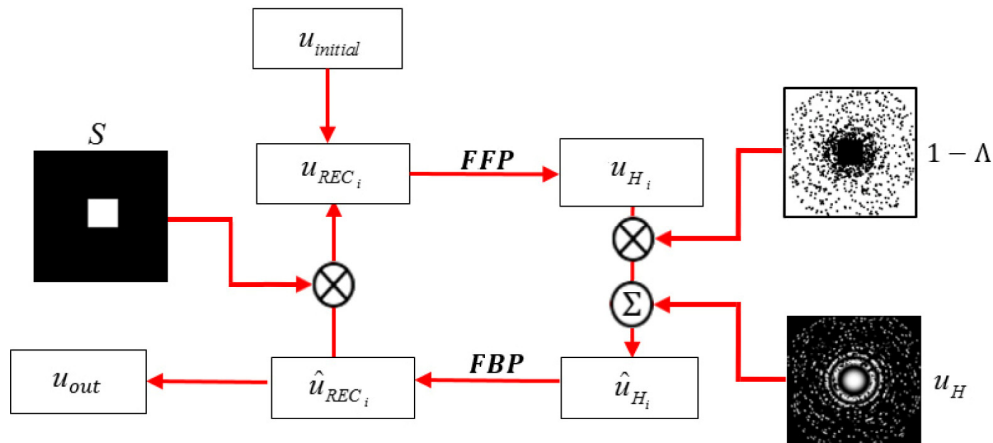


Fig. 4. Block diagram of the iterative PG algorithm.

2.3 Mosaicking considerations

A large sparse SA with minimal measurements requires a careful design of the pattern Λ . Thus, for the mosaicking process two aspects that should be taken into account are as follows:

- (i) According to the basic assumptions mentioned in section 2.1, the major amount of the intensity emitted from the test objects propagates toward the system within a relatively small angular aperture. Moreover, the CFH study [19] indicates that most of the intensity radiating from natural objects on the Fresnel hologram plane is concentrated in the central regions, whereas the intensity density decreases in the peripheral regions. Thus, the density level of the measurements should be reduced with increased radius $\sqrt{X_n^2 + Y_n^2}$ [see Fig. 2(c)].

- (ii) The ability to reconstruct a Fresnel field partially truncated by a binary mask was rigorously analyzed in [27]. The analysis indicates that optimal reconstruction results are obtained for a large number of small apertures, with respect to the total SA area, rather than a small number of large apertures.

3. Experiments and results

3.1 Numerical simulations of S-SAFE approach

In this section we analyze the S-SAFE concept and its properties with the help of six different simulations. To maintain repeatability of the simulation conditions, in every simulation the array representing the hologram plane consists of 299×299 pixels.

The first simulation [Figs. 5(a1)-5(a6)] demonstrates the ability to reconstruct an object [Fig. 5(a1)] when using only 5.22% of the hologram area. The structure of the mask [Fig. 5(a2)] representing the used area of the hologram is synthesized in accordance with the above mentioned mosaicking considerations. Therefore, for a typical objects restricted in an area of 50×50 pixels [e.g. Figure 5(a1)], the mask pattern consists of a central aperture (35×35 pixels), and peripheral apertures (8×8 pixels) that are randomly scattered in accordance with the varied density distribution mentioned in section 2.3. Figure 5(a3) shows that the central aperture acquires most of the object energy, and hence discontinuousness at the central region of the sparse hologram should be avoided, as is explained in section 2.1. Figure 5(a4) presents the corresponding FBP reconstruction of the partial hologram of Fig. 5(a3). The effects of the information loss due to the missing data at the sparse mosaic hologram are substantial. A better quality reconstruction is obtained using either the PG extrapolation [Fig. 5(a5)], or the CS approach [Fig. 5(a6)]. In both images additional details are revealed; however, under identical conditions of measurement amount and reconstruction distance, the CS approach achieves better results than the PG algorithm in the sense that more missing information of the original object is revealed.

An additional example of S-SAFE resolution capabilities is demonstrated in the second simulation [Figs. 5(b1)-5(b6)], where the tested object [Fig. 5(b1)] is a fine texture that consists of high frequencies along multiple directions. The mask pattern in Fig. 5(b2) consists of 4.32% of the hologram area, where the sizes of the central and peripheral elements are identical to those presented in the previous simulation. As before, the mask pattern is determined in accordance with the above mentioned mosaicking considerations. Figures 5(b4)-5(b6) present the corresponding FBP, PG and CS reconstructions of the sparse hologram of Fig. 5(b3), respectively. The superiority of CS over FBP and PG is demonstrated again.

In order to justify the use of the SA system, the third simulation [Figs. 5(c1)-5(c6)] simulates an equivalent FINCH system, consisting of a rectangular aperture [Fig. 5(c2)] with 4.6% of the hologram area (64×64 pixels in size), and produces a hologram [Fig. 5(c)] of the object used in the previous simulation [Figs. 5(b1) and 5(c1)]. By comparing the results of the corresponding FBP, PG and CS reconstructions [presented in Figs. 5(c4)-5(c6), respectively] to the previous simulation [Figs. 5(b4)-5(b6)], one can recognize that many of the details revealed by the S-SAFE configuration cannot be resolved using only a single limited aperture. The fourth simulation [Figs. 5(d1)-5(d6)] demonstrates the importance of the assumption that the central element of the hologram receives most of the object energy. The object of Fig. 5(a) is shifted by 20 pixels along both Cartesian directions, as shown in Fig. 5(d1). As a result of the shift, a significant portion of the light intensity overflows the central element, as is shown in Fig. 5(d3), where the mask [Fig. 5(d2)] is similar to the one presented in the first simulation [Fig. 5(a2)]. Consequently, in both reconstruction techniques [PG and CS presented in Fig. 5(d5) and 5(d6), respectively] the reconstructed images are distorted and many details are lost.

The fifth simulation [Figs. 5(e1)-5(e6)] demonstrates the importance of creating the above mentioned non-uniform, random sampling density, with respect to the distance from the

center. A uniform random sampling configuration occupying 5.7% of the aperture area is shown in Fig. 5(e2). The corresponding three reconstructions [Fig. 5(e4)-5(e6)] of the hologram of Fig. 5(e3) are distorted and most of the original details of the object are lost.

The sixth simulation [Figs. 5(f1)-5(f6)] demonstrates the importance of the randomness in the sampling pattern. In Fig. 5(f2), equal spaced peripheral elements are added to the central element, where 7.4% of the hologram area is used. As is shown in Figs. 5(f4)-5(f6), the corresponding three reconstructions of the hologram presented in Fig. 5(f3) are distorted and many of the original details of the object are lost, especially with the FBP [Fig. 5(f4)] and the PG [Fig. 5(f5)] techniques. Comparing Figs. 5(a6) and 5(f6), one can conclude that a random sampled hologram is preferred over the uniform sampled hologram, even for reconstructing the hologram with the CS algorithm.

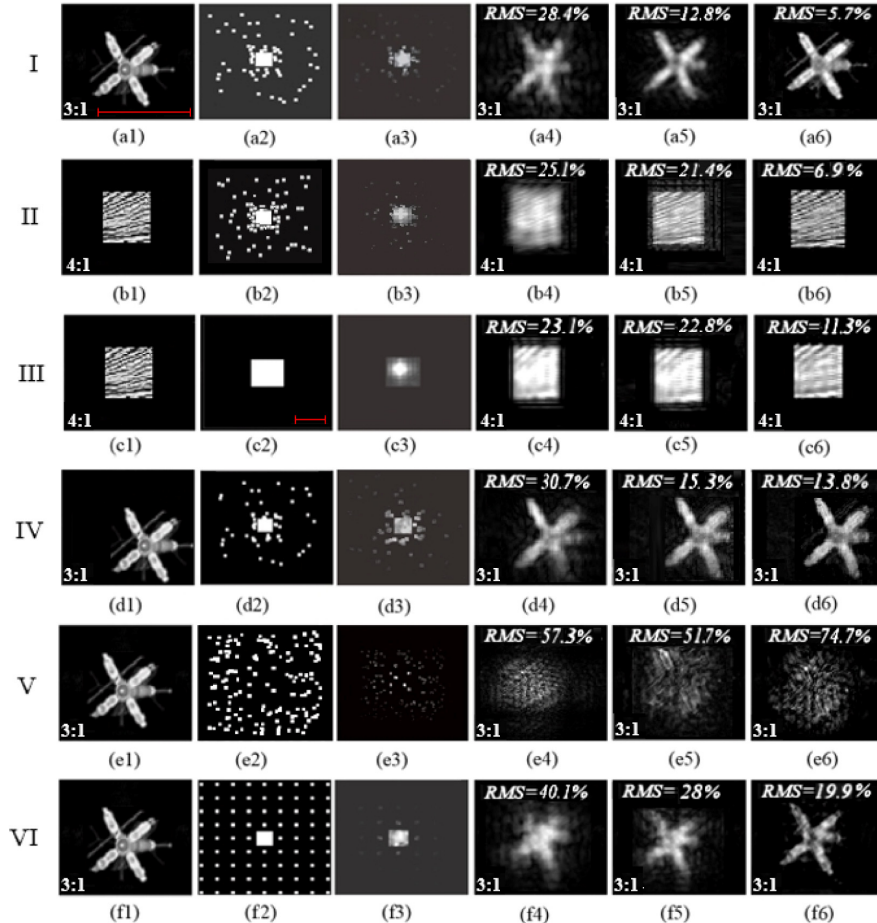


Fig. 5. Simulation results: (a1) the original object (satellite). The scale bar is 50 pixels. (a2) measurement mask that consists of 5.22% of the active area, (a3) the corresponding Fresnel hologram magnitude, (a4-a6) the reconstructed images corresponding to the hologram (a3) using (a4) FBP, (a5) PG and (a6) CS reconstructions. (b1-b6) The same as (a1-a6) for the object (land texture) of (b1) and a measurement mask (b2) of 4.32% of the active areas. (c1-c6) The same as (a1-a6) for the object of (c1) and a measurement mask (c2) of a rectangular aperture with 4.6% of the active area. The scale bar is 64 pixels. (d1-d6) The same as (a1-a6) for the out of the center object of (d1) and a measurement mask (d2) of 5.22% of the active areas. (e1-e6) The same as (a1-a6) for the object of (e1) and a measurement mask (e2) of random active areas distributed uniformly on 5.7% of the total area. (f1-f6) The same as (a1-a6) for the object of (f1) and a measurement mask (f2) of equally spaced peripheral elements mask on 7.4% of the total area.

In each reconstructed image, i.e. with the FBP, PG and CS techniques applied in every simulation, the root mean square (RMS) error between the reconstructed image and its appropriate original object is calculated according to Eqs. (18)-(20).

3.2 Experiments with sparse Fresnel holograms

In this section we compare images reconstructed from different experimentally acquired holograms digitally multiplied by various random binary masks with different percentages of the active area. The importance of this hybrid step is to examine the influence of the sparse patterns and algorithms on an experimentally acquired S-SAFE hologram. In all these experiments the size of the central element is 300×300 pixels and the peripheral sub-holograms have an area of 9×9 pixels and are randomly scattered with a density inversely proportional to the aperture radius. The FBP, CS and PG approaches are applied and compared.

As a preliminary step, a complete Fresnel hologram was recorded by a conventional FINCH system, shown in Fig. 6, with a diffractive lens of focal length $f_1 = 0.25\text{m}$, displayed on the Holoeye PLUTO SLM (1920×1080 pixels, $8\mu\text{m}$ pixel pitch, phase only modulation). The tested object is a segment of a resolution chart (RC), NBS 1963A, in which the density of the two perpendicular gratings is 25cycles/mm located in front of a collimation lens L_0 with focal length $f_0 = 0.4\text{m}$. The RC is illuminated by a LED (Thorlabs LED631E, 4mW , $\lambda = 631\text{nm}$, $\Delta\lambda = 10\text{nm}$). According to the scheme presented in Fig. 1(a), two polarizers, P_1 and P_2 , are oriented at 45° with respect to the active axis of the SLM. Next, the complete recorded hologram is *digitally* multiplied by 17 different binary masks (1080×1080 pixels) consisting of different area percentages (between 15 and 31%), where only six images are shown in Fig. 7. In order to satisfy the temporal coherence limitations, according to Eq. (21) (given in the appendix), the bandwidth of the light source should not exceed 5.33nm. Thus, the LED is filtered by a $\Delta\lambda = 1\text{nm}$ BPF.

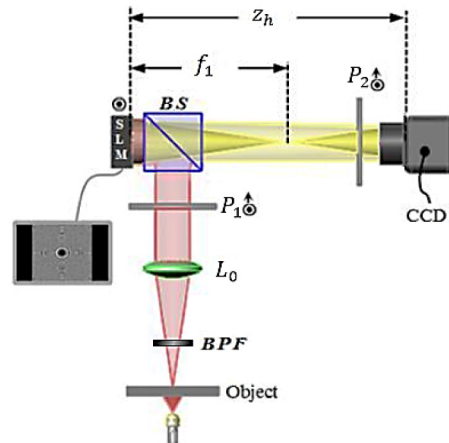


Fig. 6. Experimental setup of classical FINCH: L_0 , lens; P_1 and P_2 , polarizers; SLM, spatial light modulator; CCD, charged couple device; BS, beam splitter; BPF, bandpass filter.

The holograms are reconstructed at $z_r = 0.25\text{m}$ using FBP [Figs. 7(a1)-7(f1)], PG [Figs. 7(a2)-7(f2)] and CS [Figs. 7(a3)-7(f3)]. During this study we found empirically that applying CS reconstruction on a hologram synthesized by the PG algorithm, as an initial condition for the TwIST algorithm, provides better results than the case of choosing random initial images. Hence, the best reconstructed images using CS, shown in Figs. 7(a3)-7(f3), were obtained from a CS algorithm which was initiated with holograms computed by the PG procedure.

According to the Rayleigh criterion, to resolve a 25 cycles/mm grating on the RC located at the front focal plane of a collimating lens at a distance of 400mm, where the radiation

wavelength is 631nm, the minimal complete aperture size of a conventional incoherent imaging system should be $7.7 \times 7.7\text{mm}$ (960×960 pixels). Consequently, according to the super-resolution properties of FINCH [15], the minimal complete effective aperture required in the S-SAFE system (D_h) is about 640×640 pixels. Hence, in this experiment, the SLM marginal areas beyond the central aperture of 300×300 pixels extend the system aperture and should improve the capability to resolve the given gratings.

The average visibility of the horizontal and vertical gratings is used to evaluate the resolving power of the three reconstruction methods. The average intensities along the horizontal and vertical gratings are presented in Figs. 7(a4)-7(f4) and Figs. 7(a5)-7(f5), respectively. Figures 8(a) and 8(b) show the average visibility values of the horizontal and vertical gratings, respectively, where the blue, red and green colors represent the results of applying FBP, CS and PG, respectively.

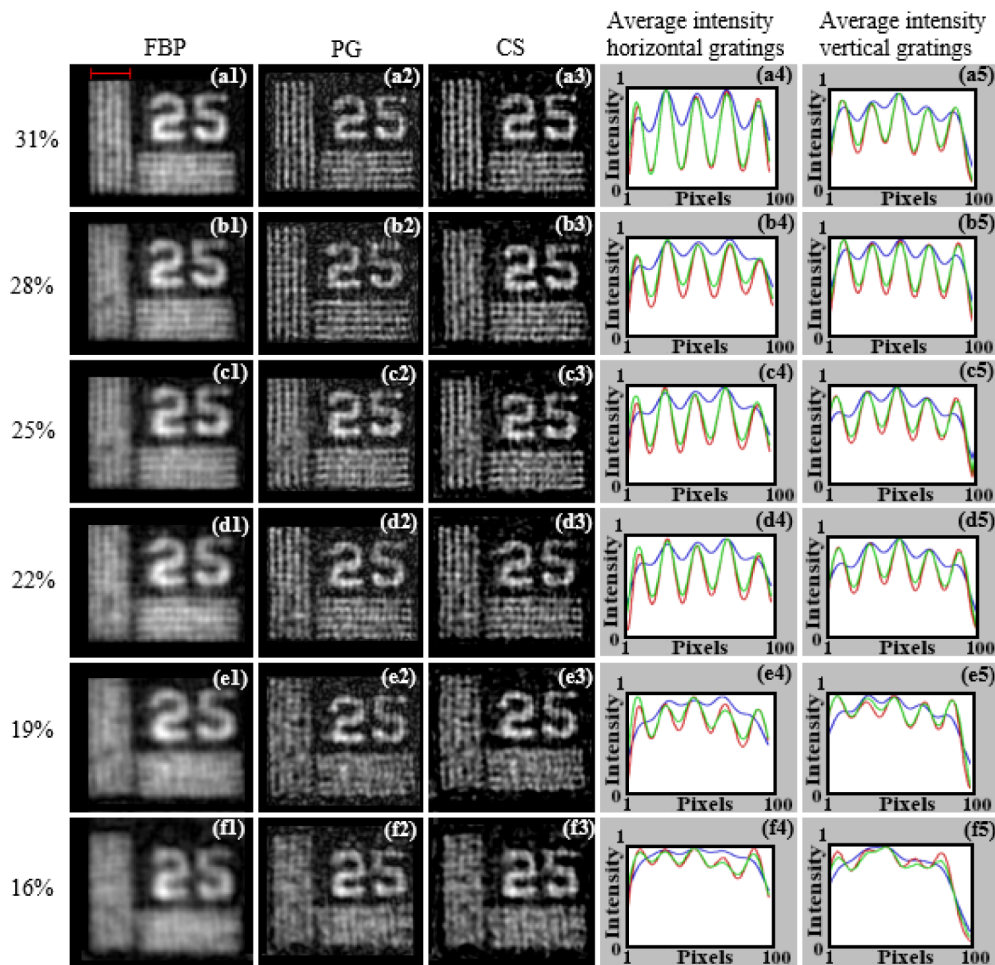


Fig. 7. Experimental results obtained by recording holograms of an RC 25 cycles/mm with different percentages of the hologram active area: (a1-f1) the images obtained with FBP with 31%-15% measurement area; (a2-f2) same as (a1-f1) for PG; (a3-f3) same as (a1-f1) for CS ; (a4-f4) the average intensity cross-sections of the three techniques along the horizontal gratings. The blue, the green and the red colors represent the FBP, PG and CS reconstructions, respectively; (a5-f5) same as (a4-f4) for the vertical gratings. The scale bar is 0.18mm.

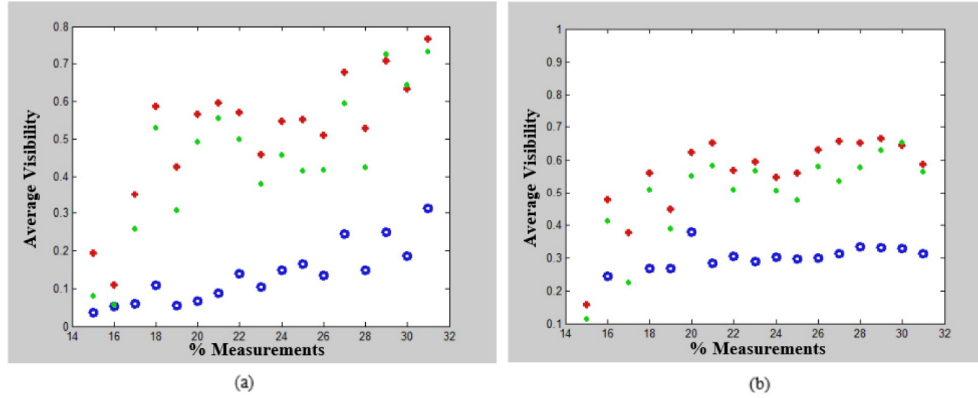


Fig. 8. Average visibility versus the percentage of the measurement area along the (a) horizontal and (b) vertical gratings. The blue rings, the green dots and the red diamonds represent the FBP, PG and CS algorithms, respectively.

3.3 S-SAFE experiment

In this subsection, we present a practical experimental procedure demonstrating the ability to reconstruct an object from a real sparse mosaic SA hologram. By creating restricted active areas on the SLM, where the opaque areas discard some of the data on the hologram plane, the final mosaic hologram only supports data in particular regions, demonstrating S-SAFE system as a realistic method. The experimental setup, illustrated in Fig. 9, was constructed using the same object, SLM, lens L_0 , polarizers P_1 and P_2 , light illumination and BPF mentioned in subsection 3.2.

First, to capture the central element, according to the schemes suggested in Figs. 1(a) and 2(a), a central quadratic phase function of 300×300 pixels is displayed on the SLM, as shown in Fig. 9(a). This central physical aperture of 2.4×2.4 mm is created with $f_1 = 0.25$ m, where the two polarizers P_1 and P_2 are oriented at 45° with respect to the active axis of the SLM.

Next, marginal Fresnel sub-holograms in random positions were recorded using the setup illustrated in Fig. 9(b). In this configuration, the polarizer P_2 is removed and the polarizer P_1 is oriented to be collinear with the active axis of the SLM, according to the scheme of Fig. 1(b). Following the scheme suggested in Fig. 2(b), a marginal rectangular quadratic element of 9×9 pixels (0.072×0.072 mm in size) is displayed on one side, whereas the symmetric area on the other side remains as a clear mirror to reflect a plane wave.

To keep the process of S-SAFE efficient, instead of processing each peripheral sub-hologram separately, they are captured together in two clusters (see Fig. 10). To implement the two marginal clusters, the following procedures have been carried out:

- (i) Two binary masks Λ_1 and Λ_2 , presented in Figs. 10(a) and 10(b), respectively, are created according to the original mask Λ . For every active area on one side there is automatically a conjugate plane mirror on the other side, since the entire other side is a plane mirror. Consequently, since the two masks Λ_1 and Λ_2 cover the entire sparse SA, the complete sparse SAFE hologram is acquired by only three steps, one for the central continuous part and another two steps for all the peripheral sparse apertures, whereas first, Λ_1 is displayed and then Λ_2 .
- (ii) The binary masks Λ_1 and Λ_2 are multiplied by two quadratic phase functions, denoted $Q_1[1/f_1]$ and $Q_2[1/f_1]$ with $f_1 = 0.25$ m, delineated by an area that represents the total position possibilities of $SLM_{1,2}$ [see Figs. 10(c) and 10(d)]. In addition, a phase shifting factor, $\exp(-i\theta)$, is introduced, in order to implement the above mentioned

phase shifting procedure. Thus, the mask displayed on the SLM can be mathematically expressed as:

$$P_{k,j}(x,y) = \Lambda_k \cdot Q_k [1/f_1] \cdot \exp(-i\theta_j), \quad (9)$$

where $k = 1,2$ represents the respective cluster of measurements and j is the index of the three exposures of the phase shifting procedure.

To tile the central element and the two clusters of sub holograms into a complete sparse mosaic hologram, the above mentioned TPCT is implemented. Because of the phase shifting procedure, it is possible to create a sparse mosaic hologram, where the data in the non-active areas does not contribute any information to the final mosaic hologram created on the CCD plane. Moreover, different positions of the conjugate peripheral apertures are obtained without any mechanical movements. Therefore, the experimental procedure is simplified and the concept can be demonstrated while using only a single SLM.

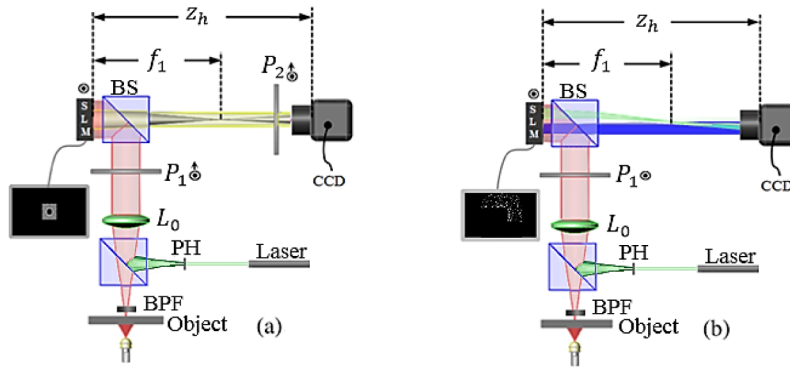


Fig. 9. Experimental setups: L_0 lens; P_1 and P_2 , polarizers; SLM, spatial light modulator; CCD, charged couple device; BS, beam splitter; BPF, bandpass filter, PH, pinhole. (a) Configuration for the central holographic element; (b) configuration for the peripheral holographic elements. The piecewise object and the pinhole are illuminated separately in two different experiments.

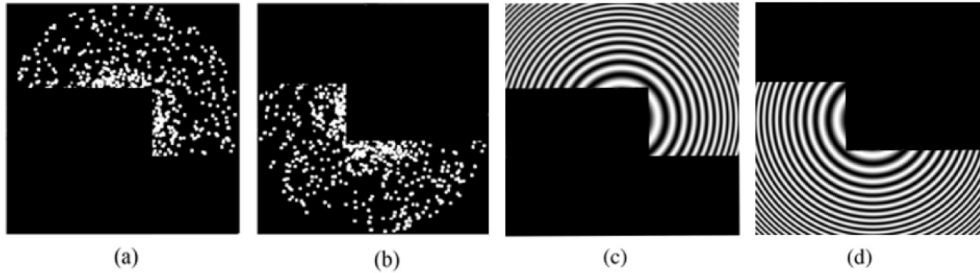


Fig. 10. (a) Mask Λ_1 of the first cluster; (b) mask Λ_2 of the second cluster; (c) the quadratic phase pattern Q_1 ; (d) the quadratic phase pattern Q_2 .

The digital binary mask Λ used for CS and for the PG algorithms represents the equivalent real effective and opaque areas on the SLM. Therefore, it is crucial to match the active areas on the SLM with the mask Λ used in the iterative digital algorithms. The relative positions between the effective areas are known in advance from the mask Λ . However, the exact lateral position and the appropriate scaling of the total mask with respect to the hologram plane must be adjusted. Thus, the ability to expose the real measurement distribution is essential.

To expose the pattern of the active areas on the SLM, and to match it for use on the hologram plane, we repeat the same acquisition process by recording a hologram of a pinhole,

illuminated by a HeNe laser ($\lambda = 633\text{nm}$). Reconstruction of the SLM pattern, by implementing FBP on this hologram along a distance of $2z_r = 0.5\text{m}$, reveals the real structure of the binary mask Λ . Therefore, a new calibrated mask $\tilde{\Lambda}$, which fits the real measurements, is obtained by performing scaling and lateral shifts on the original mask Λ , so the active areas overlap with the actual mask obtained from the experiment [see Fig. 11 (b)]. In other words, a reference plane wave [represented by the green beam in Figs. 9(a) and 9(b)] is used in order to match the real sparse aperture, created on the SLM, to the original design; by this procedure we achieve an appropriate convergence of the iterative reconstruction algorithms.

The hologram is now ready for application of the numerical algorithms with the reconstruction distance of $z_r = 0.25\text{m}$ and the new binary mask for the algorithms is $\tilde{\Lambda}$.

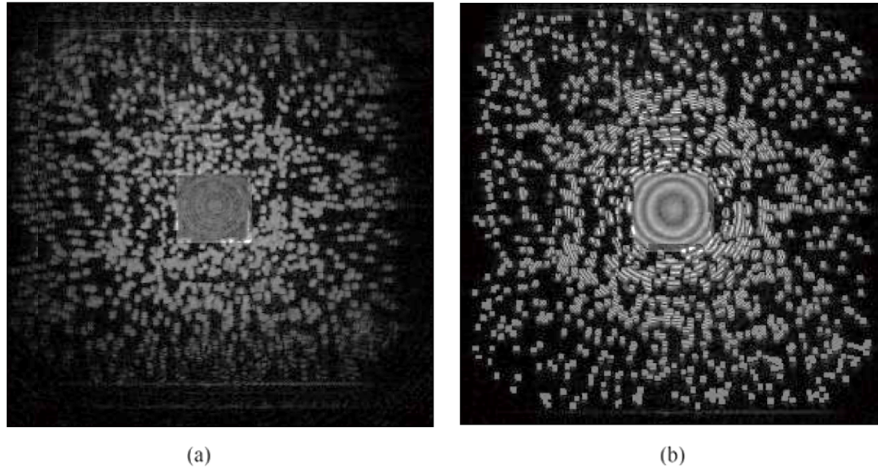


Fig. 11. (a) The active areas revealed by reconstructing the SLM plane illuminated by a laser; (b) the calibrated digital mask $\tilde{\Lambda}$ matched to the actual measurements.

In the experiment, a partial mosaic hologram of 30% measurements was created by the S-SAFE system, and is reconstructed according to the above described techniques. Figure 12(a) presents the results of the FBP reconstruction, in which it is easy to see that the vertical and horizontal gratings are distorted and the digits are blurred, due to the missing high frequency data in the sparse hologram.

Figure 12(b) presents the results of the PG algorithm, where some of the details are more clearly revealed (for instance part of the horizontal lines). Figure 12(c) presents the results of the CS algorithm, where the PG results were used as an initial condition for the CS process, as was done in the previous experiment. The best image quality and maximum sharpness are obtained in Fig. 12(c). Moreover, a significant improvement also occurs in the average visibility of the two gratings, as shown in Figs. 12(e)-12(h). In order to demonstrate the importance of the peripheral measurements for the SA method, Fig. 12(d) presents, for a comparison, a reconstructed object obtained by FBP of the central element (size of 300×300 pixels) only.

Based on the simulations presented in section 3.1, the ability to resolve image details reconstructed by a sparse mosaic hologram is conditioned by following the mosaicking rules outlined in section 2.3. Moreover, in order to achieve a high quality reconstructed image, a minimal amount of measurements is required (depending on the object complexity), as predicted by CS theory. However, from the experiment described in this section we conclude that, in practice, many additional challenges and limitations should be taken into consideration as well; e.g. inaccurate interferograms arrangements, distortions that occur due

to the finite size of the apertures and mismatching between the measurement positions and the designed binary mask Λ .

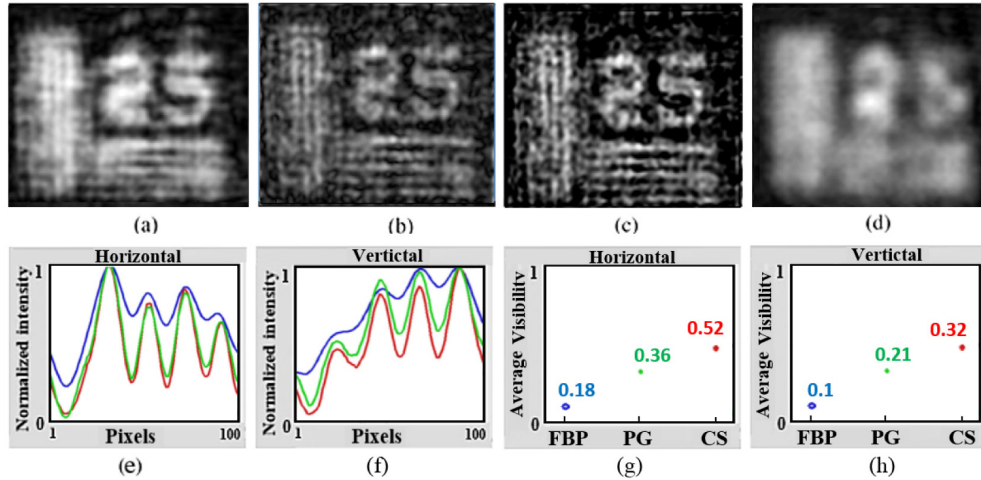


Fig. 12. Experimental results obtained by recording an S-SAFE hologram with 30% of the SA area: (a),(b),(c) the images obtained by FBP, PG and CS, respectively; (d) The image obtained by FBP of the central element; (e), (f) the average cross-sections of the three techniques along the horizontal and vertical gratings, respectively. The blue, the green and the red colors represent the FBP, PG and CS reconstructions, respectively; (g), (h) average visibility corresponding to the three techniques along the horizontal and vertical gratings, respectively.

4. Conclusions

In this study we have presented an advanced SAFE system that, in spite of its limited resources, still produces an image with super resolution qualities. The S-SAFE configuration generates a large scale sparse SA, in which the effects due to missing data can be compensated for by implementing optimization techniques, as long as a certain mosaicking structure is applied.

The S-SAFE method was analyzed through the comparison of three reconstruction approaches; FBP, CS and PG. The comparative numerical simulation indicates that a high quality image can be reconstructed from only about 5% of the aperture area. In the second experiment, a complete hologram of an object was recorded by a FINCH system and reconstructed after digitally multiplying the hologram by 17 different binary masks with different percentages of the active area. Based on the comparison between the three reconstruction methods, we conclude that a high resolution reconstructed image can be obtained from a sparse FINCH hologram and the reconstruction quality is improved by increasing the percentages of the active area. In most cases CS has some advantage over PG, however, to improve the CS results further, the PG can be used for generating the initial data of the CS. In the third experiment, the S-SAFE system was tested by creating a real sparse hologram, defined by active areas sparsely distributed over the SLM. In this procedure many additional challenges and limitations were taken into consideration and resolved through different techniques, which were presented and explained.

In summary, a large scale SA implemented by the S-SAFE concept has two main advantages;

- (i) The sparse mosaic hologram is composed from a relatively small amount of sub-elements and, consequently, its information capacity is significantly lower than with regular SAFE.

- (ii) The holographic elements are not constrained to any particular position and, therefore, the calibration requirements of the system are less severe than for regular SAFE.

Thus, one can recognize that S-SAFE is an innovative approach that practically provides the ability to perceive small details using a sparse, instead of a monolithic, SA.

Acknowledgment

This work was supported by The Israel Ministry of Science and Technology (MOST), by The Israel Science Foundation (ISF) (Grant No. 439/12) and by the National Institutes of Health (NIH), National Institute of General Medical Sciences Award Number U54GM105814.

Appendix

In this appendix we provide a mathematical analysis of the S-SAFE system, based on previous studies of SAFE [10,13,14]. Consider an object composed of spatially incoherent point sources, each emitting a quasi-monochromatic spherical wave. The complex amplitude induced just before the lens L_0 by one arbitrary object point, located at $(x_s, y_s, -f_0)$ with an amplitude of $\sqrt{I_s}$, is expressed as $\sqrt{I_s}C(\bar{r}_s)L(-\bar{r}_s/f_0)Q(1/f_0)$, where f_0 is the focal length of the lens L_0 [Fig.1(a)], Q designates the quadratic phase function of the form: $Q(b) = \exp[i\pi b\lambda^{-1}(x^2 + y^2)]$, λ is the central wavelength of the light source, L denotes the linear phase function of the form: $L(\bar{s}) = \exp[i2\pi\lambda^{-1}(s_x x + s_y y)]$, and $C(\bar{r}_s)$ is a complex constant dependent on the location of the point source. The spherical wave is collimated by the lens L_0 . As the plane wave meets a single SLM for the central sub-hologram [Fig.1(a)], or two SLMs for the marginal sub-holograms [Fig. 1(b)], the wave splits into two truncated waves, where one of them is modulated by a quadratic phase element. Thus, taking into consideration that the sizes of the central SLM and of the two SLMs (for the marginal sub-holograms) are different, the input complex amplitude in the n_{th} exposure is multiplied by the function $T_n(x, y; \theta_j)$, representing a general random sparse pattern with a continuous central element as follows:

$$T_n(x, y; \theta_j) = \begin{cases} C_1 Q\left(\frac{-1}{f_1}\right) \exp(i\theta_j) \text{rect}\left(\frac{x}{A_x}, \frac{y}{A_y}\right) + C_2 \text{rect}\left(\frac{x}{A_x}, \frac{y}{A_y}\right) & n = 0 \\ C_1 Q\left(\frac{-1}{f_1}\right) \exp(i\theta_j) \text{rect}\left(\frac{x - X_n}{\tilde{A}_x}, \frac{y - Y_n}{\tilde{A}_y}\right) + C_2 \text{rect}\left(\frac{x + X_n}{\tilde{A}_x}, \frac{y + Y_n}{\tilde{A}_y}\right) & \text{Otherwise,} \end{cases} \quad (10)$$

where f_1 is the focal distance of the converging spherical wave relative to the SLM plane, C_1 and C_2 are constants and θ_j is one of the three angles used for phase shifting in order to eliminate the twin image and the bias terms from the final hologram [11,12,15,16]. The physical aperture of the SLMs is described as a rectangular function:

$$\text{rect}\left(\frac{x}{\xi}, \frac{y}{\eta}\right) \equiv \begin{cases} 1 & (|x|, |y|) \leq (\xi/2, \eta/2) \\ 0 & \text{otherwise} \end{cases}$$

Beyond the SLM plane, the two waves propagate in free space over an additional distance z_h . Thus, under the Fresnel approximation, the complex amplitude is convolved with the

function $Q(1/z_h)$. Finally, the magnitude of the interference pattern is squared in order to yield the intensity distribution, recorded by the CCD. Hence, a complete Fresnel hologram of the object point located at $(x_s, y_s, -f_0)$ is given as a sum of N sub-holograms, as follows:

$$I(\bar{r}_0; \bar{r}_s; \theta_j) = \sum_{n=0}^N \left| \sqrt{I_s} C(\bar{r}_s) L\left(\frac{-\bar{r}_s}{f_0}\right) Q\left(\frac{1}{f_0}\right) Q\left(-\frac{1}{f_0}\right) * Q\left(\frac{1}{d}\right) \right. \\ \left. \times T_n(x, y; \theta_j) * Q\left(\frac{1}{z_h}\right) \right|^2, \quad (11)$$

where the asterisk denotes a 2D convolution, $\bar{r}_0 = (x_0, y_0)$ is the location vector of the CCD plane, N is the total number of measurements and $T_n(x, y; \theta)$ is given by Eq. (10). In order to eliminate the twin image and the bias term, in every n_{th} position three holograms are recorded and superimposed with three different values of θ_j [12,13,16,17]. Following previous calculations presented in [10], Eq. (11) can be written in the form:

$$I(\bar{r}_0; \bar{r}_s; \theta_j) = \left(C_3 + C_4(\bar{r}_s) Q\left(-\frac{1}{z_r}\right) L\left(\frac{-\bar{r}_r}{z_r}\right) \exp(-i\theta_j) + \right. \\ \left. C_4^*(\bar{r}_s) Q\left(\frac{1}{z_r}\right) L\left(\frac{\bar{r}_r}{z_r}\right) \exp(i\theta_j) \right) \times \left\{ \text{rect}\left(\frac{x}{A_x}, \frac{y}{A_y}\right) + \sum_{n=1}^N \text{rect}\left(\frac{x-X_n}{\tilde{A}_x}, \frac{y-Y_n}{\tilde{A}_y}\right) \right\}, \quad (12)$$

where C_3 and C_4 are constants and z_r is the reconstruction distance from the hologram (CCD plane) to the reconstructed image point, given by

$$z_r = \pm \frac{z_h}{2}. \quad (13)$$

The vector $\bar{r}_r = (x_r, y_r)$ is the transversal location of the reconstructed image point, given by

$$\bar{r}_r = (x_r, y_r) = \left(\frac{x_s z_h}{f_0}, \frac{y_s z_h}{f_0} \right). \quad (14)$$

The transverse magnification is expressed as $M_T = \partial x_r / \partial x_s = z_h / f_0$ and is the same as the magnification of conventional FINCH [12].

Consider an effective aperture $D_E \gg \tilde{A}_x, \tilde{A}_y$ and taking into consideration that N represents the most distant position of the SLM couple, the total diameter D_E of the effective aperture can be described as $D_E = 2\sqrt{\max_n(X_n^2 + Y_n^2)}$. From Fig. 1(b), one can recognize that the above mentioned external boundary of the partial mosaic hologram is the diameter D_H illustrated in Fig. 2(c), equal to the maximal diameter of the effective aperture, and thus,

$$D_H = 2\sqrt{X_N^2 + Y_N^2}. \quad (15)$$

Assuming that the mosaic hologram is a circle, where D_H is its diameter, the angular resolution limit of the S-SAFE system for a complete mosaic hologram is:

$$\Delta\theta_{MIN} = \frac{1}{2} \frac{2\lambda z_r}{M_T D_H f_0}, \quad (16)$$

where the resolution limit of the FINCH based system is half of that of any equivalent conventional coherent imaging system [12–16]. Substituting the magnification and Eqs. (13) and (15) into Eq. (16), where $z_h = 2f_1$, yields that the angular resolution is:

$$\Delta\theta_{MIN} = \frac{\lambda}{4\sqrt{X_N^2 + Y_N^2}}. \quad (17)$$

However, since the S-SAFE approach consists of a sparse mosaic hologram, i.e. incomplete NA, the practical value of the angular resolution is smaller than the value given in Eq. (17). One might get as close as possible to the value $\Delta\theta_{MIN}$ by forming an optimal measurement pattern and using an appropriate reconstruction algorithm.

According to Ref [28], measuring the difference between two compared images (e.g. the reconstructed image and the original image) is enabled by calculating the RMS error \bar{e}_{rms} as follows:

$$\bar{e}_{rms} = \frac{e^{1/2}}{MAX_{mn} |\tilde{f}_{mn}|}, \quad (18)$$

where \tilde{f}_{mn} represents the desired object, and e represents the mean square error between the images given by

$$e = \frac{1}{MN} \sum_m^M \sum_n^N |\tilde{f}_{mn} - \gamma \bar{h}_{mn}|^2, \quad (19)$$

where \bar{h}_{mn} represents the reconstructed image and the minimization constant γ is calculated as:

$$\gamma = \frac{\sum_m^M \sum_n^N \tilde{f}_{mn} \bar{h}_{mn}^*}{\sum_m^M \sum_n^N |\bar{h}_{mn}|^2}. \quad (20)$$

The BPF in all the SAFE systems is aimed to increase the temporal coherence and by that to increase the visibility of the recorded holograms. In order to choose an appropriate BPF, one needs to ensure that the maximal optical path difference (OPD) between the above mentioned plane and spherical waves, is shorter than the coherence length of the light. The coherence length is approximately the ratio $\lambda^2/\Delta\lambda$, where $\Delta\lambda$ is the spectral bandwidth and λ is the central wavelength of the light. For an effective aperture of D_H , the maximal OPD between the waves is $\Delta_{OPD} = \sqrt{z_h^2 + D_H^2} - 2f_1$. Thus, the required upper limit of the spectral band-pass is:

$$\Delta\lambda < \frac{\lambda^2}{\sqrt{4f_1^2 + D_H^2} - 2f_1}. \quad (21)$$